THz Conductivity of Semiconducting 2H and Metallic 1T Phases of Molybdenum Disulfide

Matt D. Capobianco¹, Sabrina M. Younan², Uriel Tayvah¹, Brian Pattengale¹, Jens Neu¹, Jing Gu², Gary W. Brudvig^{1,*}

¹Department of Chemistry and Yale Energy Sciences Institute, Yale University, New Haven, Connecticut 06520-8107, United States

²Department of Chemistry and Biochemistry, San Diego State University, San Diego, California 92182-1030, United States

AUTHOR INFORMATION

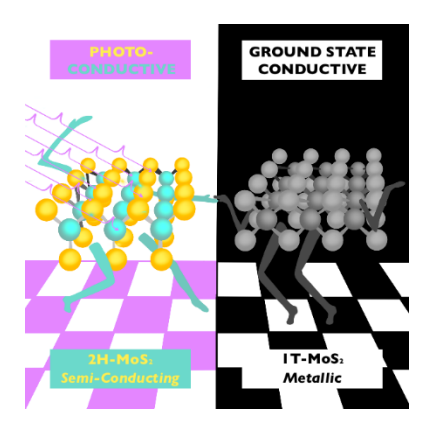
Corresponding Author

gary.brudvig@yale.edu

ABSTRACT

Molybdenum disulfide (MoS₂) has been extensively studied in its commonly occurring semiconducting 2H phase. Recent synthetic advances have enabled the bulk synthesis of the catalytically promising metallic 1T phase. However, the conductivity of bulk 1T-MoS₂ has not been well characterized to ascertain the carrier transport properties. Terahertz (THz) spectroscopy is an ideal technique for obtaining this crucial information because it is a non-contact method of measuring the conductivity of emerging materials with ultrafast time resolution. This work applies THz spectroscopy to bulk 2H-MoS₂ and 1T-MoS₂, representing the first application of the technique on the 1T phase, with measurements confirming the semiconducting character of 2H-MoS₂ and the metallic character 1T-MoS₂. This study provides new insight into the metallic nature of bulk 1T-MoS₂ and a direct comparison to the semiconducting 2H phase that, together with physical characterization to obtain and material parameters, are important to optimize applications in catalysis devices, and beyond.

TOC GRAPHICS



KEYWORDS 2D Materials, Terahertz Spectroscopy, Ultrafast Spectroscopy, Materials Physics, Catalysis, Conductivity

2D materials are of keen interest because of their novel electronic and catalytic properties. They can also serve as modular building blocks, with easy manipulation of the number of layers in samples from a bulk form to a single layer due to relatively weak Van der Waals interactions between the stacked layers in the third dimension; which also allows for easy construction of heterostructures. ^{1,2} 2D materials exist in forms that exhibit properties of semiconductors, metals, superconductors, and insulators. ^{1,3} Within the same chemical composition, the change in number of layers or the way the atoms are oriented can cause a drastic difference in the electronic structure of these materials. ^{3,4}

The 2H semiconducting phase of MoS₂ (2H-MoS₂) has been studied extensively for applications including transistors, batteries, and photocatalysis.^{5–9} 2H-MoS₂ photocatalytic properties have been leveraged to perform hydrogen evolution, pollutant degradation, uranium extraction, and much more.^{7,9,10} Despite significant progress and research in the past decades, pure 2H-MoS₂ has yet to reach a desired photocatalytic efficacy.^{11,12} This is thought to be because the active catalysis sites are found only on edge sites while the more abundant basal plane sites are inactive.^{11,12} Several approaches to overcome this shortcoming have been explored, including increasing the number of active sulfur vacancies and edges, combining it with other 2D materials in a heterostructure, and incorporating a co-catalyst.^{2,5,11,12}

Previous approaches achieved a moderate improvement in catalytical efficiency but at the cost of adding expensive co-catalysts or complicating the MoS₂ synthesis. Striving for homogenous catalysis based on earth abundant materials, researchers turned to the 1T phase of MoS₂ (1T-MoS₂), which has been found to be metallic.^{13–15} In the 1T phase, the sulfur atoms are

trigonal prismatically coordinated around the Mo atoms, whereas in the semiconducting 2H phase they are hexagonally coordinated.^{16,17} 1T-MoS₂ is metastable and is commonly calcinated with ions, such as NH₄⁺ and Li⁺, for stabilization.^{13,18} In this work, stable bulk 1T-MoS₂ is synthesized by a hydrothermal method without the addition of a harsh metal cation. As with the 2H phase, the 1T phase has applications in areas such as photocatalysis and batteries, but exhibits a greatly improved efficacy.^{15,19} The 1T phase also has the potential to replace precious metals, such as Pt and Ir, as a co-catalyst in many catalytic processes.^{20,21}

Conductive electrons are believed to be responsible for the improved performance of 1T-MoS₂ as compared to the 2H-phase in catalysis. However, prior works have not quantitatively measured this conductivity improvement, nor have they validated the metallic nature of catalytically-relevant bulk 1T-MoS₂. Terahertz (THz) spectroscopy is a sub-picosecond technique that is sensitive to conductive, or mobile, charge carriers making it useful to study photoactive materials such as 2D materials. Most methods to measure conductivity, such as DC conductivity, require contacts to the sample being measured, which can alter the structure of the sample and complicate the interpretation of the results. THz spectroscopy has the advantage of being a non-contact method, making it an ideal technique to quantitatively access the conductivity of bulk 2D materials. As a conductivity of bulk 2D materials.

THz spectroscopy enables one to measure the high-frequency AC conductivity of the sample of interest. The AC conductivity obtained by THz spectroscopy is particularly relevant to catalytic materials owing to its frequency being commensurate with carrier diffusion distances. THz time-domain spectroscopy (THz-TDS) measures the electric field of THz pulse as it passes through a sample.^{22,23} By comparing this pulse with a pulse passed through a known reference, the complex refractive index can be extracted.^{22,24,25} The complex conductivity is calculated from the

complex refractive index and with fitting can yield parameters such as carrier density and effective mass of the carriers.²³ Low frequency phonons can contribute to the complex refractive index as well.^{22,23}

Since photocatalysis with MoS₂ materials is also of interest, it is critical to be able to track the dynamics of conductive carriers after photoexcitation. Optical-pump THz-probe (OPTP) combines THz-probe radiation with an optical pump beam to monitor the ultrafast change in THz attenuation due to visible excitation; this change is directly proportional to the photoconductivity.^{23,26,27} OPTP generates dynamics datasets that can be modeled to extract decay information related to photoinduced processes.²⁶ Time-resolved THz spectroscopy (TRTS) also combines THz radiation and a visible pump but measures the frequency-dependent photoconductivity at a given time delay.^{23,26} Fitting the frequency-dependent complex conductivity (or photoconductivity) with models such as the Drude model or modified versions thereof gives insight into the carrier density and scattering lifetimes.^{26,28,29}

THz spectroscopy is widely used in the field of 2D materials, where it has been applied to graphene, carbon nitride, MXenes, transition metal dichalcogenides, among others.^{23,26,30,31} To date, THz studies on MoS₂ have only focused on the 2H phase, specifically with samples that range from one to few-layers.^{32–35} Herein, we present the first use of THz spectroscopy on bulk 1T-MoS₂ and the first comparative study to 2H-MoS₂. Our THz-TDS measurements yield results consistent with a semiconducting material for 2H-MoS₂ and a metallic character for 1T-MoS₂. OPTP shows a much larger photoconductivity for 2H-MoS₂, compared to 1T-MoS₂ which exhibits a relatively weak and short-lived photoconductivity consistent with its metallic character. An even more detailed understanding of the charge carriers is gained from TRTS measurements which show that the carrier scattering is more pronounced in the 1T phase compared to 2H-MoS₂. The comparative

results herein provide crucial insight into the conductivity properties of bulk 1T- and 2H-MoS₂. These results validate the metallic nature of bulk 1T-MoS₂, which underlines its excellent catalytic performance.

Characterization of 2H-MoS₂ and 1T-MoS₂

Raman spectroscopy was employed to compare the behavior of interlayer phonon modes present in the 2H and 1T phases of MoS₂ (Fig. 1a); the assignments of the Raman peaks are labeled in Fig. 1a. Fundamentally, Raman signatures of different polymorphs demonstrate distinct differences, such as the appearance/disappearance of phonon modes, shifted peak positions, and changes to peak widths. 36 In 2H-MoS₂, two of the three peaks present are assigned to the $\rm E^{1}_{2g}$ (383 cm⁻¹) and A_{1g} (408 cm⁻¹) phonon modes that correspond to in-plane and out-of-plane Mo-S vibrations, respectively.³⁷ The 2LA (451 cm⁻¹) peak arises from the two-phonon scattering of longitudinal acoustic (LA) phonons at the M point of the Brillouin zone.³⁷ In 1T-MoS₂, the E^{1}_{2g} (376 cm⁻¹) and A_{1g} (402 cm⁻¹) peaks exhibit inverse peak intensities and broadening. Additionally, the appearance of new phonon modes in the 100-350 cm⁻¹ region indicates the presence of defects. Altogether, these observations indicate that the hydrothermally synthesized MoS₂ predominantly exists in the 1T phase.³⁸ Powder XRD patterns were also collected to further confirm the purity of the MoS₂ polymorphs (Fig. 1b). The diffraction patterns of 1T-MoS₂ and 2H-MoS₂ were indexed to Powder Diffraction File (PDF) #01-075-1539 (tetragonal 1T-MoS₂, P3m1) and PDF #01-07-1508 (hexagonal 2H-MoS₂, P6₃/mmc), respectively.³⁹ The narrow peak widths produced by 2H-MoS₂ demonstrate the crystalline nature of 2H-MoS₂. In contrast, the extreme peak broadening observed for 1T-MoS₂ reveals the amorphous nature of hydrothermally grown 1T-MoS₂. The lack of crystallinity in 1T-MoS₂ is consistent with the presence of defect-induced Raman signatures as

well. Based on these results, we deduce that 2H-MoS₂ retains a crystalline structure with hexagonal layer symmetry and 1T-MoS₂ exhibits a more amorphous structure with tetragonal layer symmetry.

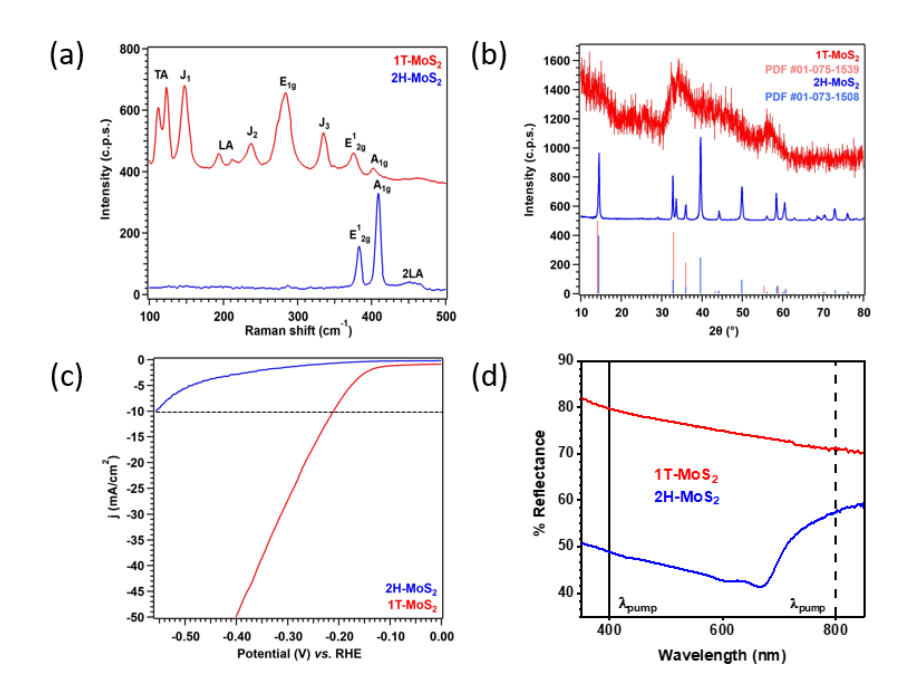


Figure 1. (a) Raman Spectroscopy of 1T-MoS₂ (red) and 2H-MoS₂ (blue); the resonances are labeled with the appropriate modes confirming the structure of the polymorphs. (b) XRD patterns for 1T-MoS₂ (red) and 2H-MoS₂ (blue); calculated peak positions are shown in the faded corresponding colors, confirming the structure of the polymorphs. (c) LSVs in acidic electrolyte of 1T-MoS₂ (red) and 2H-MoS₂ (blue); the dashed line shows that 1T-MoS₂ requires a lower overpotential to give a current density of -10 mA/cm⁻¹ for the hydrogen evolution reaction (HER). (d) Diffuse Reflective UV-Visible spectra of 1T-MoS₂ (red) and 2H-MoS₂ (blue) with the corresponding excitation wavelengths for pump-probe THz measurements indicated with lines at 400 nm (solid black) and 800 nm (dashed black). The broad absorption range emphasizes that

MoS₂ is well suited for sun-light driven chemistry. The powder samples were mixed with non-absorbing BaSO₄ for reflectance measurements.

To understand how conductivity impacts catalytic activity towards the hydrogen evolution reaction (HER), linear sweep voltammograms (LSVs) of the MoS₂ polymorphs were measured (Fig. 1c). The LSVs were measured electrochemically in acidic electrolyte (N₂-saturated 0.5 M H₂SO₄) within a three-electrode cell configuration (see Methods for more information). Comparison of the overpotentials measured at -10 mA/cm² (dashed line, Fig, 1c) of each polymorph yields significantly different results. While 2H-MoS₂ produces a large overpotential of -558 mV (vs. RHE), 1T-MoS₂ yields a much lower overpotential of -211 mV. Since overpotential is a measurement of the amount of applied energy required to drive a nonspontaneous reaction forward, this significant decrease in overpotential indicates that 1T-MoS₂ requires less than half the amount of applied energy to drive HER than 2H-MoS₂.

Ground State Conductivity Using THz-TDS

THz-TDS was measured to investigate the steady-state THz-properties of the 2H and 1T phases and examine the ground-state conductivity difference. As shown in Fig. 2a, the real part of the complex refractive index (\hat{n}) for 2H-MoS₂ has a value just below three and is relatively frequency and temperature independent. The imaginary part, also displayed in Fig. 2a, has a value that is just above zero and is also frequency and temperature independent. The real and imaginary parts of the refractive index being relatively temperature independent indicate that 2H-MoS₂ is a semiconducting material.⁴⁰ The measured refractive index is consistent with previous reports.^{33,34} The conductivity (σ) is related to the refractive index by $\hat{\varepsilon} = \varepsilon_L + \frac{i\sigma}{\omega\varepsilon_0}$ where $\hat{\varepsilon}$ is the permittivity which is equal to \hat{n}^2 , ω is the radial frequency, and ε_L is the minimum lattice (assumed to be one).

The real part of the conductivity is displayed in Fig. 2c. For the 2H phase, the conductivity decreases with lower temperature which is to be expected for a semiconducting material due to a decreased thermal electron occupation of the conduction band at lower temperatures. Al, As seen in Fig. 2b, the imaginary part of \hat{n} for 1T-MoS₂ is larger than the real part which is a hallmark of a metallic-like material. The conductivity, Fig. 2d, for 1T-MoS₂ increases with lower temperature which we attributed to decreased electron-phonon scattering at low temperature as the phonons are frozen out. The 1T phase has a higher conductivity than the 2H phase which is to be expected based on the lower overpotential required to drive HER for 1T-MoS₂. THz-TDS therefore identifies bulk 2H-MoS₂ as semiconducting and bulk 1T-MoS₂ as metallic which is consistent with previous reports.

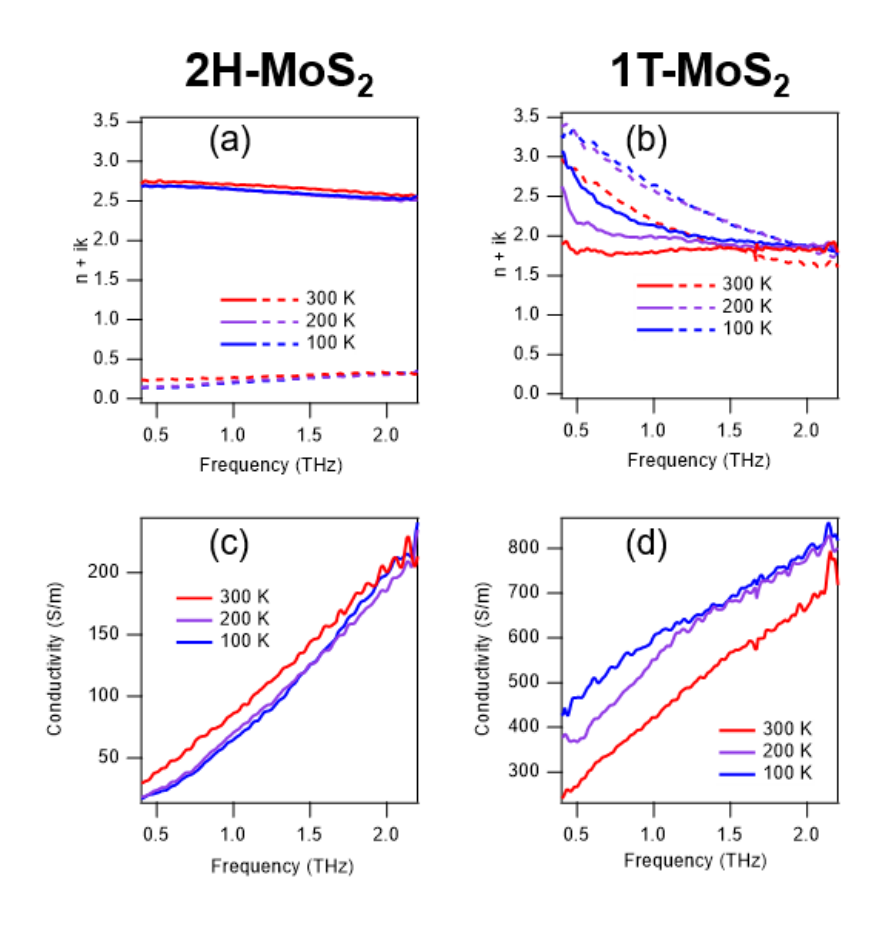


Figure 2. Real (solid) and imaginary (dashed) refractive index and conductivity of 2H-MoS₂ (a,c) and 1T-MoS₂ (b,d) at three temperature: 300 K (red), 200 K (purple), and 100 K (blue).

Ultrafast Photoconductivity Dynamics

Photocatalysis is driven by long-lived carriers; OPTP is an excellent technique to monitor the processes that effect the lifetime of mobile carriers, such as trapping and recombination. UV-Visible measurements (Fig. 1d) show a broad absorption from 350 nm to 850 nm; therefore, to understand the difference in photoconductivity between "hot" electrons with surplus energy (400 nm excitation) and electrons generated at an energy closer to the band edge (800 nm excitation), OPTP measurements were performed at both 400 nm and 800 nm excitation and are shown in Fig. 3. The observed ΔTHz from OPTP measurements can be attributed to free carriers and not excitons since conductivity requires a net charge.²³ For the signal seen in 2H-MoS₂, a biexponential equation (eq. 1) yielded excellent fits which are consistent with previously reported transient absorption measurements.^{45,46}

$$\Delta THz = \left(A_1 e^{\frac{t}{\tau_1}} + A_2 e^{\frac{t}{\tau_2}} \right) \otimes G_r(FWHM) \tag{1}$$

 A_x and τ_x are the amplitude and lifetime of the respective process and $G_r(FWHM)$ is the Gaussian instrument response function. The two exponentials can be attributed to the trapping of electrons at surface states and phonon assisted recombination, respectively, with the latter being the slower process. ^{45,46} The global fits show that the lifetimes for trapping are 6.8 ± 0.3 ps and 7.5 ± 0.4 ps for 800 nm and 400 nm respectively, and that the phonon assisted recombination lifetimes are 48

 \pm 1 ps and 44 \pm 2 ps for 800 nm and 400 nm, respectively, consistent with previously reported transient absorption measurements.⁴⁵

Under strong photoexcitation conditions often used in ultrafast laser experiments, electronelectron interactions, photo-damage, and bleaching effects may dominate. Thus, measurements using these experimental conditions may not give a reliable approximation of the lower fluences for solar photocatalysis. To understand the influence of high photon fluxes on the photoconductivity of MoS₂, we performed OPTP measurements at multiple pump powers. Figs. 3a and 3c show the OPTP data for 800 nm and 400 nm excitation, respectively, at different pump fluences. In order to look at the magnitude of each relaxation pathway as function of pump power, a global fit was done fixing the lifetimes but allowing the amplitudes of components to vary. For the 2H phase, the relationship between the pump power and peak THz amplitude is non-linear for both excitation wavelengths (Fig. S5), which can be attributed to a non-linear process such as absorption saturation. A previous report from Kar et al. showed this relationship to be linear for a few-layer sample of 2H-MoS₂ only at pump fluences on the lower end of the range of fluence used here; therefore, our observation is consistent with the prior results.³⁴ The normalized traces (Fig. S6) show a longer-lived photoconductivity component for high pump powers which is also seen as the ratio of A₁/A₂ from the global fit becomes smaller (Fig. S7) at higher pump powers. This observation is consistent with saturation of non-mobile trap states: at higher fluence, traps states fill up, and carriers can only lose their mobility by the slower phonon assisted recombination process. These trends are observed for both 400 nm and 800 nm excitation. When comparing the different excitation energies but the same photon flux (Fig. S8), there is no significant difference in the dynamics for the two excitation wavelengths.

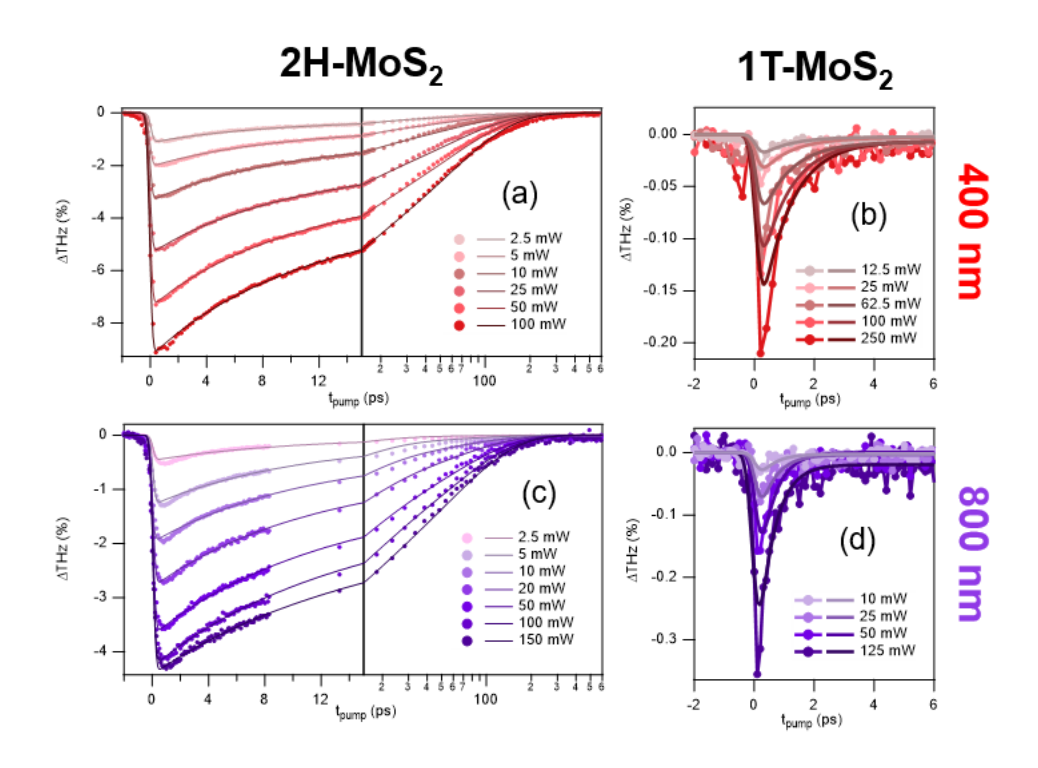


Figure 3. Pump-Dependence OPTP plot of 2H-MoS₂ (a,c) and 1T-MoS₂ (b,d) with the given photo fluxes at 400 nm (a.b) and 800 nm (c,d) excitation. The data are shown as dots and the corresponding biexponential fits are shown as solid lines. The pump powers are shown in the legend next to their corresponding data and fits. It should be noted that the y-axes are on different scales and the OPTP signal of the 2H phase is an order of magnitude larger than that of the 1T phase.

Phonon assisted recombination depends on the phonon density, which in turn is directly related to the sample temperature. OPTP measurements were, therefore, made at various temperatures to further explore the recombination mechanism. In addition to the room temperature measurements (300 K), traces were collected at 200 K and 100 K (Fig. S9). OPTP traces were collected at both 400 nm and 800 nm excitation wavelengths as well as at different pump powers. Global fits were done at each excitation wavelength and temperatures; the resulting fit parameters

are tabulated in the SI. At all three temperatures, a leveling off of the peak ΔTHz is observed as the pump fluence is increased (Fig. S10). As the pump power is increased (Fig. S10), there is a larger relative amplitude in the carrier-phonon component which again can be attributed to the saturation of trap states. There is a temperature dependence on the lifetime of the phonon assisted recombination for both excitation wavelengths (Fig. S11). For both excitation wavelengths, as the temperature decreases, a longer lifetime is observed for the phonon-carrier scattering which we attribute to the decreased phonon population at those temperatures. There is not a significant trend seen for the temperature dependence of the trapping pathway which is to be expected since a change in temperature should not affect the trapping sites owing to the trap energies exceeding the thermal energy.

OPTP measurements were made for the 1T phase as well but yielded signals that were much smaller in magnitude and shorter in lifetime, which is to be expected due to the metallic character of the 1T phase. Figs. 3b and 3d displays the peak THz attenuation versus delay time, for different pump powers, for both 800 nm and 400 nm excitation respectively. The maximum amplitude scaled linearly with pump power (Fig. S5) contrary to the saturation observed in the 2H phase. Global fits were performed with a single exponential function (eq. 2), where A corresponds to the amplitude of the component and τ corresponds to the lifetime which was held equal for all pump powers. The fit gave lifetimes of 1.0 ± 0.2 ps and 0.45 ± 0.06 ps for excitation at 800 nm and 400 nm, respectively.

$$\Delta THz = \left(Ae^{\frac{t-t_0}{\tau}}\right) \otimes G_r(FWHM) \tag{2}$$

Similarly short lifetimes have also been observed for conductive polymers.⁴⁷ Just as with the THz-TDS results, the OPTP results confirm that 2H-MoS₂ is semiconducting and 1T-MoS₂ is metallic.

Frequency Resolved Photoconductivity

Beyond OPTP, further information can be gained from measuring the frequency dependent complex photoconductivity using TRTS. In order to deliver quantitative results, TRTS measurements require a precisely known sample geometry. Teflon – commonly used in TDS measurements – could not be used since Teflon absorbs at the pump wavelength. Instead, a thin film was formed using a Nafion suspension as previously reported.⁴⁸ TRTS measurements were collected 1 ps after photoexcitation for both phases to allow for a comparison between the 2H phase and the short-lived excitation in the 1T phase. The complex-valued photoconductivity was calculated using the thin-film approximation (eq. 3)

$$\hat{\sigma}(\omega) = \frac{n_n + 1}{Z_0 d_n} \left(\frac{1}{T(\omega)} - 1 \right) \tag{3}$$

where Z_0 is the impedance of free space, d_p is the penetration length, n_n is the refractive index of the non-photoexcited material, and T is the experimental transmission.⁴⁹ The extracted photoconductivity for the 2H and 1T phases for 400 nm and 800 nm excitation, are displayed in Fig. 4. In order to match the photon flux for both excitation wavelengths for the 1T phase, the measurements were performed using 100 mW for 400 nm excitation and 50 mW for 800 nm excitation. For the 2H phase, the measurements were performed using 5 mW for 400 nm excitation and 2.5 mW for 800 nm excitation within the previously determined linear regime while also matching the photon flux. There are no apparent resonances in the frequency range for either

excitation wavelength for either phase. The shaded regions represent the standard deviations for measurements on three different samples.

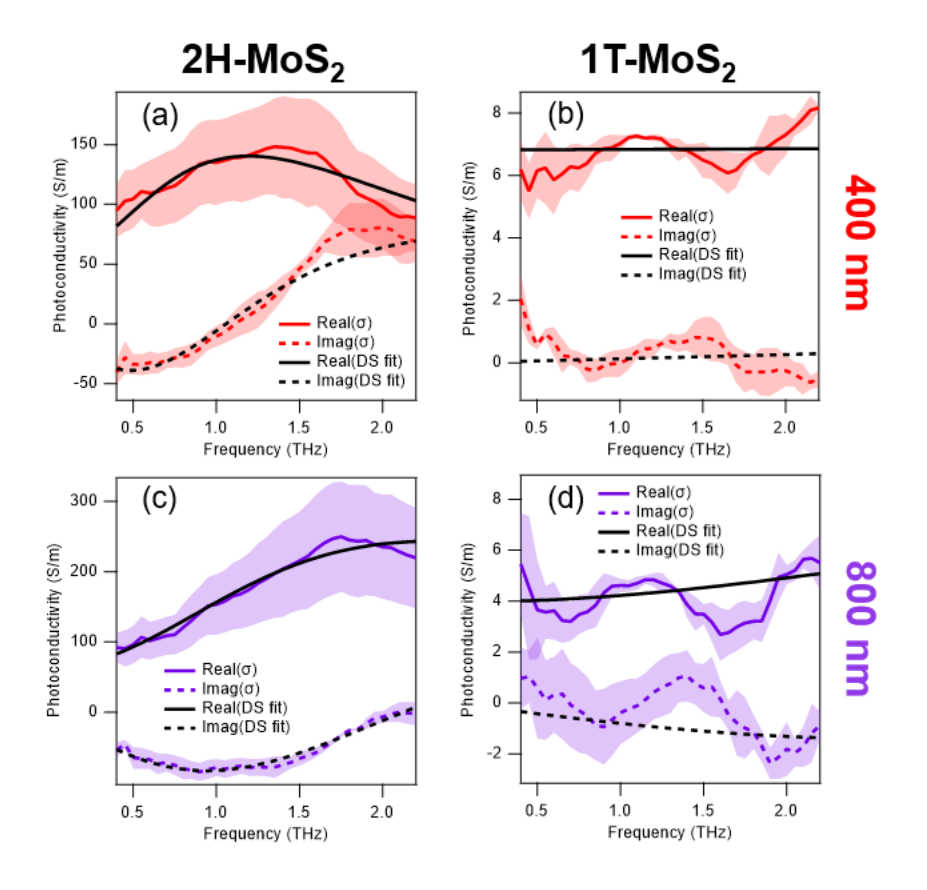


Figure 4. Frequency Dependent photoconductivity of 2H-MoS₂ (a,c) and 1T-MoS₂ (b,d) at 1 ps after photoexcitation, for 800 nm (a,b) and 400 nm (c,d) excitation with standard deviations shaded.

The Drude-Smith model was fitted to the data (eq. 4) to quantify the observed photoconductivity.

$$\hat{\sigma}(\omega) = \frac{\sigma_0}{1 - i\omega\tau_{DS}} \left(1 + \frac{c}{1 - i\omega\tau_{DS}} \right) \tag{4}$$

Within the Drude-Smith model, σ_0 is the DC-photoconductivity, τ_{DS} is the scattering lifetime and c, referred to as the c-parameter, is a measure of the persistence of velocity. ²⁹ A c-parameter of 0 corresponds to full randomization of the velocity during scattering events; this is most commonly

seen in single crystals. In contrast, a c-parameter of -1 suggests that carriers simply reverse their direction during scattering events, which is consistent with scattering at the boundaries of electrically separated crystallites. The frequency dependent photoconductivity was measured for three duplicates for each wavelength and phase, and a global fit was performed where τ_{DS} and the c-parameter were the same for all three duplicates and σ_0 was allowed to float for the three samples to account for variations in sample preparation. The resulting fits are displayed in black in Fig. 4 for all four plots and the resulting fit parameters are shown in Table 1 (confidence intervals are shown in Table S10 and S11).

Table 1. Parameters from Drude-Smith Fit. 95 % credible intervals are shown in Tables S10 and S11.

	Excitation Wavelength (nm)	σ_0 (S/m)	$ au_{DS}$ (ps)	<i>c</i> -parameter
2H-MoS ₂	800	278	0.119	-0.813
	400	484	0.0644	-0.868
1T-MoS ₂	800	11.4	0.00903	-0.401
	400	14.8	0.0197	-0.732

As expected from the OPTP data presented earlier, a much larger σ_0 is observed for the 2H phase compared to the 1T phase. For the 1T phase, there is no significant change in the scattering lifetime between the two different excitation wavelengths; both times are much shorter than for the 2H phase. For the 2H phase, the scattering time using 800 nm excitation is twice as long as that seen using 400 nm excitation which could be due to electrons being injected into states well above the conduction band minimum when the higher energy excitation is used. This surplus energy can open novel scattering channels and generate phonons which in turn could scatter with mobile

electrons. Interestingly, this surplus energy does not influence the charge transfer between grains, which can be seen from the excitation wavelength independence of the c-parameter. For the 1T phase, the c-parameter is closer to 0 for 800 nm excitation meaning that when less energy is introduced to the electrons, they boundaries are not causing as many scattering events.

We present the first application of THz spectroscopy on metallic 1T-MoS₂, which was performed in comparison to semiconducting 2H-MoS₂. Each sample was measured in bulk form which has further never been reported for 2H-MoS₂. THz-TDS yielded ground-state conductivities consistent with semiconductor character for the 2H phase and metallic character for the 1T phase. For 2H-MoS₂, a large OPTP photoconductivity signal was observed that was modeled with a biexponential function with the decay components being attributed to trapping into non-conductive states and phonon assisted recombination, respectively. Pump-fluence dependence and temperature dependent OPTP measurements supported the assignment of these two relaxation processes. For 1T-MoS₂, a small and very short-lived OPTP signal is observed when compared to the semiconducting phase, providing further evidence of its metallic character. Overall, this study provides important insight on the difference in ground state conductivity and photoconductivity of the commonly occurring semiconducting 2H-MoS₂ and the emerging metallic 1T-MoS₂. Such insights are critical toward understanding and further developing high-performance metallic 1T-MoS₂ catalysts.

ASSOCIATED CONTENT

Supporting Information.

The following files are available free of charge.

Methods section; description and schematic of laser tables, THz-TDS data analysis methods, and statistical methods for error analysis; Complex refractive index of individual spots from THz-TDS measurements; OPTP measurements at 200 K and 100 K for 2H-MoS₂, normalized OPTP traces for both phases (and each temperature for 2H-MoS₂), comparisons of lifetimes from exponential fits at various temperatures, peak ΔTHz versus pump power for OPTP measurements, and ratio of the two components from the double exponential fit for 2H-MoS₂ at various temperatures; fit results and error analysis for global fits for OPTP and TRTS measurements; XRD, Raman, and OPTP of MoS₂ films with and without Nafion and explanation of observed differences. This material is available free of charge via the Internet at http://pubs.acs.org.

AUTHOR INFORMATION

Notes

The authors declare no competing financial interests.

ACKNOWLEDGMENT

This work was supported by the U.S. National Science Foundation (Grant CHE-1954453). Jing Gu acknowledges NSF CBET-1704992 to support this research. U.T. acknowledges the support of the National Science Foundation Graduate Research Fellowship (DGE-1752134). The authors would like to acknowledge Sarah Ostresh for creating the TOC.

REFERENCES

- Hynek, D. J.; Pondick, J. V.; Cha, J. J. The Development of 2D Materials for Electrochemical Energy Applications: A Mechanistic Approach. *APL Mater.* 2019, 7 (3), 030902.
- (2) Hu, W.; Yang, J. Two-Dimensional van Der Waals Heterojunctions for Functional Materials and Devices. *J. Mater. Chem. C* **2017**, *5* (47), 12289–12297.
- (3) Chaves, A.; Azadani, J. G.; Alsalman, H.; da Costa, D. R.; Frisenda, R.; Chaves, A. J.; Song, S. H.; Kim, Y. D.; He, D.; Zhou, J.; Castellanos-Gomez, A.; Peeters, F. M.; Liu, Z.; Hinkle, C. L.; Oh, S.-H.; Ye, P. D.; Koester, S. J.; Lee, Y. H.; Avouris, Ph.; Wang, X.; Low, T. Bandgap Engineering of Two-Dimensional Semiconductor Materials. *Npj 2D Mater. Appl.* **2020**, *4* (1), 29.
- (4) Zhang, G.; Huang, S.; Wang, F.; Yan, H. Layer-Dependent Electronic and Optical Properties of 2D Black Phosphorus: Fundamentals and Engineering. *Laser Photonics Rev.* 2021, 15 (6), 2000399.
- (5) Li, X.; Zhu, H. Two-Dimensional MoS₂: Properties, Preparation, and Applications. *J. Materiomics* **2015**, *I* (1), 33–44.
- (6) Zhu, Z.; Mosallanezhad, A.; Sun, D.; Lei, X.; Liu, X.; Pei, Z.; Wang, G.; Qian, Y.
 Applications of MoS₂ in Li–O₂ Batteries: Development and Challenges. *Energy Fuels*2021, 35 (7), 5613–5626.
- (7) Zhu, J.; Wang, Z.-C.; Dai, H.; Wang, Q.; Yang, R.; Yu, H.; Liao, M.; Zhang, J.; Chen, W.; Wei, Z.; Li, N.; Du, L.; Shi, D.; Wang, W.; Zhang, L.; Jiang, Y.; Zhang, G. Boundary Activated Hydrogen Evolution Reaction on Monolayer MoS₂. *Nat. Commun.* **2019**, *10* (1), 1348.

- (8) Hinnemann, B.; Moses, P. G.; Bonde, J.; Jørgensen, K. P.; Nielsen, J. H.; Horch, S.; Chorkendorff, I.; Nørskov, J. K. Biomimetic Hydrogen Evolution: MoS₂ Nanoparticles as Catalyst for Hydrogen Evolution. *J. Am. Chem. Soc.* **2005**, *127* (15), 5308–5309.
- (9) Lai, M. T. L.; Lee, K. M.; Yang, T. C. K.; Pan, G. T.; Lai, C. W.; Chen, C.-Y.; Johan, M. R.; Juan, J. C. The Improved Photocatalytic Activity of Highly Expanded MoS₂ under Visible Light Emitting Diodes. *Nanoscale Adv.* 2021, 3 (4), 1106–1120.
- (10) Wang, Y.; Wang, J.; Liang, J.; Pan, D.; Li, P.; Fan, Q. Efficient Recovery of Uranium from Saline Lake Brine through Photocatalytic Reduction. *J. Mol. Liq.* **2020**, *308*, 113007.
- (11) Li, H.; Tsai, C.; Koh, A. L.; Cai, L.; Contryman, A. W.; Fragapane, A. H.; Zhao, J.; Han, H. S.; Manoharan, H. C.; Abild-Pedersen, F.; Nørskov, J. K.; Zheng, X. Activating and Optimizing MoS₂ Basal Planes for Hydrogen Evolution through the Formation of Strained Sulphur Vacancies. *Nat. Mater.* **2016**, *15* (3), 364–364.
- (12) Li, L.; Qin, Z.; Ries, L.; Hong, S.; Michel, T.; Yang, J.; Salameh, C.; Bechelany, M.; Miele, P.; Kaplan, D.; Chhowalla, M.; Voiry, D. Role of Sulfur Vacancies and Undercoordinated Mo Regions in MoS₂ Nanosheets toward the Evolution of Hydrogen. ACS Nano 2019, 13 (6), 6824–6834.
- (13) Liu, Q.; Li, X.; He, Q.; Khalil, A.; Liu, D.; Xiang, T.; Wu, X.; Song, L. Gram-Scale

 Aqueous Synthesis of Stable Few-Layered 1T-MoS₂: Applications for Visible-Light-Driven

 Photocatalytic Hydrogen Evolution. *Small* **2015**, *11* (41), 5556–5564.
- (14) Sun, D.; Huang, D.; Wang, H.; Xu, G.-L.; Zhang, X.; Zhang, R.; Tang, Y.; Abd EI-Hady, D.; Alshitari, W.; Saad AL-Bogami, A.; Amine, K.; Shao, M. 1T MoS₂ Nanosheets with

- Extraordinary Sodium Storage Properties via Thermal-Driven Ion Intercalation Assisted Exfoliation of Bulky MoS2. *Nano Energy* **2019**, *61*, 361–369.
- (15) Shi, S.; Sun, Z.; Hu, Y. H. Synthesis, Stabilization and Applications of 2-Dimensional 1T Metallic MoS₂. *J. Mater. Chem. A* **2018**, *6* (47), 23932–23977.
- (16) Enyashin, A. N.; Yadgarov, L.; Houben, L.; Popov, I.; Weidenbach, M.; Tenne, R.; Bar-Sadan, M.; Seifert, G. New Route for Stabilization of 1T-WS₂ and MoS₂ Phases. *J. Phys. Chem. C* **2011**, *115* (50), 24586–24591.
- (17) Jernigan, G. G.; Fonseca, J. J.; Cress, C. D.; Chubarov, M.; Choudhury, T. H.; Robinson, J. T. Electronic Changes in Molybdenum Dichalcogenides on Gold Surfaces. *J. Phys. Chem. C* 2020, *124* (46), 25361–25368.
- (18) Wu, J.; Liu, J.; Cui, J.; Yao, S.; Ihsan-Ul-Haq, M.; Mubarak, N.; Quattrocchi, E.; Ciucci, F.; Kim, J.-K. Dual-Phase MoS₂ as a High-Performance Sodium-Ion Battery Anode. *J. Mater. Chem. A* **2020**, *8* (4), 2114–2122.
- (19) Huang, Y.; Sun, Y.; Zheng, X.; Aoki, T.; Pattengale, B.; Huang, J.; He, X.; Bian, W.; Younan, S.; Williams, N.; Hu, J.; Ge, J.; Pu, N.; Yan, X.; Pan, X.; Zhang, L.; Wei, Y.; Gu, J. Atomically Engineering Activation Sites onto Metallic 1T-MoS₂ Catalysts for Enhanced Electrochemical Hydrogen Evolution. *Nat. Commun.* 2019, 10 (1), 982.
- (20) Joe, J.; Bae, C.; Kim, E.; Ho, T. A.; Yang, H.; Park, J. H.; Shin, H. Mixed-Phase (2H and 1T) MoS₂ Catalyst for a Highly Efficient and Stable Si Photocathode. *Catalysts* **2018**, *8* (12), 580.
- (21) Liang, Z.; Guo, Y.; Xue, Y.; Cui, H.; Tian, J. 1T-Phase MoS ₂ Quantum Dots as a Superior Co-Catalyst to Pt Decorated on Carbon Nitride Nanorods for Photocatalytic Hydrogen Evolution from Water. *Mater. Chem. Front.* **2019**, *3* (10), 2032–2040.

- (22) Neu, J.; Schmuttenmaer, C. A. Tutorial: An Introduction to Terahertz Time Domain Spectroscopy (THz-TDS). *J. Appl. Phys.* **2018**, *124* (23), 231101.
- (23) Spies, J. A.; Neu, J.; Tayvah, U. T.; Capobianco, M. D.; Pattengale, B.; Ostresh, S.; Schmuttenmaer, C. A. Terahertz Spectroscopy of Emerging Materials. *J. Phys. Chem. C* **2020**, *124* (41), 22335–22346.
- (24) Neu, J.; Schmuttenmaer, C. A. Terahertz Spectroscopy and Density Functional Theory Investigation of the Dipeptide L-Carnosine. *J. Infrared Millim. Terahertz Waves* 2020, 41 (11), 1366–1377.
- (25) Yasuda, H.; Hosako, I. Measurement of Terahertz Refractive Index of Metal with Terahertz Time-Domain Spectroscopy. *Jpn. J. Appl. Phys.* **2008**, *47* (3), 1632–1634.
- (26) Capobianco, M. D.; Pattengale, B.; Neu, J.; Schmuttenmaer, C. A. Single Copper Atoms Enhance Photoconductivity in G-C₃N₄. *J. Phys. Chem. Lett.* **2020**, *11* (20), 8873–8879.
- (27) Pattengale, B.; Neu, J.; Ostresh, S.; Hu, G.; Spies, J. A.; Okabe, R.; Brudvig, G. W.; Schmuttenmaer, C. A. Metal–Organic Framework Photoconductivity via Time-Resolved Terahertz Spectroscopy. *J. Am. Chem. Soc.* **2019**, *141* (25), 9793–9797.
- (28) Cocker, T. L.; Baillie, D.; Buruma, M.; Titova, L. V.; Sydora, R. D.; Marsiglio, F.; Hegmann, F. A. Microscopic Origin of the Drude-Smith Model. *Phys. Rev. B* **2017**, *96* (20), 205439.
- (29) Smith, N. Classical Generalization of the Drude Formula for the Optical Conductivity. *Phys. Rev. B* **2001**, *64* (15), 155106.
- (30) Han, P.; Wang, X.; Zhang, Y. Time-Resolved Terahertz Spectroscopy Studies on 2D Van Der Waals Materials. *Adv. Opt. Mater.* **2020**, *8* (3), 1900533.

- (31) Pattengale, B.; G. Freeze, J.; J. Guberman-Pfeffer, M.; Okabe, R.; Ostresh, S.; Chaudhuri, S.; S. Batista, V.; A. Schmuttenmaer, C. A Conductive Metal–Organic Framework Photoanode. *Chem. Sci.* 2020, *11* (35), 9593–9603.
- (32) Docherty, C. J.; Parkinson, P.; Joyce, H. J.; Chiu, M.-H.; Chen, C.-H.; Lee, M.-Y.; Li, L.-J.; Herz, L. M.; Johnston, M. B. Ultrafast Transient Terahertz Conductivity of Monolayer MoS₂ and WSe₂ Grown by Chemical Vapor Deposition. ACS Nano 2014, 8 (11), 11147– 11153.
- (33) Arcos, D.; Gabriel, D.; Dumcenco, D.; Kis, A.; Ferrer-Anglada, N. THz Time-Domain Spectroscopy and IR Spectroscopy on MoS₂. *Phys. Status Solidi B* **2016**, *253* (12), 2499–2504.
- (34) Kar, S.; Su, Y.; Nair, R. R.; Sood, A. K. Probing Photoexcited Carriers in a Few-Layer MoS₂ Laminate by Time-Resolved Optical Pump-Terahertz Probe Spectroscopy. ACS Nano 2015, 9 (12), 12004–12010.
- (35) Yang, Y.; He, C.; Huang, Y.; Zhu, L.; Zhou, Y.; Xu, X. Ultrafast Terahertz Complex Conductivity Dynamics of Layered MoS₂ Crystal Probed by Time-Resolved Terahertz Spectroscopy. *Front. Phys.* **2021**, *9*, 1–7.
- (36) Le Pevelen, D. D.; Tranter, G. E. *FT-IR and Raman Spectroscopies, Polymorphism Applications*; Elsevier: Cambridge, UK 2017
- (37) Tan, P.-H. *Raman Spectroscopy of Two-Dimensional Materials*; Springer Berlin Heidelberg: New York, NY, 2018.
- (38) Friedman, A. L.; Hanbicki, A. T.; Perkins, F. K.; Jernigan, G. G.; Culbertson, J. C.;
 Campbell, P. M. Evidence for Chemical Vapor Induced 2H to 1T Phase Transition in MoX₂
 (X = Se, S) Transition Metal Dichalcogenide Films. *Sci. Rep.* 2017, 7 (1), 3836.

- (39) Gates-Rector, S.; Blanton, T. The Powder Diffraction File: A Quality Materials Characterization Database. *Powder Diffr.* **2019**, *34* (4), 352–360.
- (40) Hervé, P. J. L.; Vandamme, L. K. J. Empirical Temperature Dependence of the Refractive Index of Semiconductors. *J. Appl. Phys.* **1995**, *77* (10), 5476–5477.
- (41) Dallas, P.; Stamopoulos, D.; Boukos, N.; Tzitzios, V.; Niarchos, D.; Petridis, D.
 Characterization, Magnetic and Transport Properties of Polyaniline Synthesized through
 Interfacial Polymerization. *Polymer* 2007, 48 (11), 3162–3169.
- (42) Meissner, W. Thermische und elektrische Leitfähigkeit einiger Metalle zwischen 20 und 373° abs. *Ann. Phys.* **1915**, *352* (16), 1001–1058.
- (43) Yasuda, H.; Measurement of Terahertz Refractive Index of Metals. 2008 Asia-Pacific Microwave Conference; 2008, 1–4.
- (44) Ma, F.-Y.; Su, J.-P.; Gong, Q.-X.; Yang, J.; Du, Y.-L.; Guo, M.-T.; Yuan, B. Measurement of the Optical Constants of Thin Metal Films by THz Differential Time Domain Spectroscopy. *Chin. Phys. Lett.* **2011**, *28* (9), 097803.
- (45) Wang, H.; Zhang, C.; Rana, F. Ultrafast Dynamics of Defect-Assisted Electron–Hole Recombination in Monolayer MoS₂. *Nano Lett.* **2015**, *15* (1), 339–345.
- (46) Tsai, H.-S.; Huang, Y.-H.; Tsai, P.-C.; Chen, Y.-J.; Ahn, H.; Lin, S.-Y.; Lu, Y.-J. Ultrafast Exciton Dynamics in Scalable Monolayer MoS₂ Synthesized by Metal Sulfurization. *ACS Omega* **2020**, *5* (19), 10725–10730.
- (47) Esenturk, O.; Kline, R. J.; Delongchamp, D. M.; Heilweil, E. J. Conjugation Effects on Carrier Mobilities of Polythiophenes Probed by Time-Resolved Terahertz Spectroscopy. *J. Phys. Chem. C* **2008**, *112* (29), 10587–10590.

- (48) Spies, J. A.; Hilibrand, M. J.; Neu, J.; Ostresh, S.; Swierk, J. R.; Schmuttenmaer, C. A. Suspensions of Semiconducting Nanoparticles in Nafion for Transient Spectroscopy and Terahertz Photoconductivity Measurements. *Anal. Chem.* **2020**, *92* (6), 4187–4192.
- (49) Neu, J.; Regan, K. P.; Swierk, J. R.; Schmuttenmaer, C. A. Applicability of the Thin-Film Approximation in Terahertz Photoconductivity Measurements. *Appl. Phys. Lett.* **2018**, *113* (23), 233901.